Advanced Steel Construction – Vol. 22 No. 2 (2026) 130–142
DOI:10.18057/IJASC.2026.22.2.1

EXPERIMENTAL AND NUMERICAL ANALYSIS ON THE STRUCTURAL PROPERTIES OF CONCRETE-FILLED RECTANGULAR THIN-WALLED HIGH-STRENGTH STAINLESS-STEEL TUBULAR COLUMNS

Jun Zhao [1], Yang Peng [2], Wei-Chao Zhang [3], Shen-Lan Li [4] and Jun Dong [2,*]

[1] *School of Civil Engineering and Architecture, Changzhou Institute of Technology, Changzhou 213032, China*
[2] *College of Civil Engineering, Nanjing Tech University, Nanjing 211816, China*
[3] *Sinopec Sales Co., Ltd. Lianyungang Petroleum Branch, Lianyungang 222500, China*
[4] *Rural Economic Service Center of Banpu Town, Lianyungang 222241, China*
** (Corresponding author: E-mail: dongjun@njtech.edu.cn)*

ABSTRACT

Exploring high-performance structures suitable for high corrosion marine environment is one of the research priorities in engineering. In order to meet the requirements of the marine environment and reduce costs, thin-walled stainless-steel was used to design a high-performance component. Two stainless-steel lipped channels were welded to form a new stainless-steel tubular column, with concrete filled inside, a high-performance concrete-filled stainless-steel tubular column was designed. Axial compression short column test, finite element analysis of axial compression short columns, axial compression and compression-bending intermediate-length columns were carried in the paper. Six groups of axial compression tests were conducted, results shown that both rectangular stiffening ribs and V-shaped stiffening ribs could enhance the restraint capacity of the external stainless-steel tube. The ultimate capacity of the axial compression short column with bidirectional ribs was 15.04% higher than that of the short column with unidirectional ribs. The axial compression mechanization of short columns, axial compression and compression-bending mechanization of median long column were analyzed by FEM. For axial compression short columns, the main parameters were the size of the V-shaped stiffeners and the compressive strength of the concrete. When the width-to-thickness ratio of the V-shaped stiffener was 8.33 and the angle was 90°, the cross-sectional performance was the best. When the concrete was C80, the peak load was increased by 17.20% compared with C60. For axial compression and compression-bending intermediate-length columns, the main parameters were the slenderness ratio and eccentricity. When the slenderness ratio was in the range of 15.17-91.02, the larger the slenderness ratio, the faster the stiffness degradation. When the eccentricity was in the range of 0.56-3.75, the deformation capacity of intermediate-length columns was better, and the ductility was also better. The recommendation of compression-bending capacity calculation formula was proposed, with high accuracy.

ARTICLE HISTORY

Received: 20 February 2025
Revised: 21 June 2025
Accepted: 26 June 2025

KEYWORDS

High-strength stainless-steel;
Concrete-filled rectangular tubular column;
Axial compression short column test;
Compression-bending;
Finite element analysis

Copyright © 2026 by The Hong Kong Institute of Steel Construction. All rights reserved.

1. Introduction

Seawater and ocean currents could easily cause corrosion and impact, restricting the development of marine engineering [1-3]. High-strength stainless-steel had good mechanical properties and corrosion resistance, which could meet the highly corrosive environmental conditions and reduce the maintenance cost [4-5]. Welding the lipped channels and assembled into a rectangular section, with concrete filled inside, a better performance component with bidirectional ribs could formed [6-8]. It had advantages of light self-weight, strong corrosion resistance and large capacity compared with concrete-filled steel tube [9-10].

Scholars have carried out related experiments and theoretical research on concrete-filled steel tube for decades [11-13]. Lai et al. [14] collected the test data of 41 groups of axial compression short columns, 17 groups of compression-bending members and 4 groups of pure bending members with thin-walled and non-compact sections of concrete-filled steel tubes. A finite element numerical model was established to determine the applicability of AISC 360 for calculating rectangular thin-walled concrete-filled steel tube components. Aslani et al. [15] collected 316 groups of test data of axial compression short columns and axial compression long columns of rectangular and square concrete-filled steel tubes, and calculated the applicability of the Australian design code to the axial compression capacity of high-strength concrete-filled steel tube components. Liew et al. [16] conducted compression-bending experiments on square high-strength steel tube columns. With ultra-high-strength concrete filled inside, the calculated values of the test and different steel reduction factors were calculated. The results showed that high-strength concrete-filled steel tubes could be designed and calculated using the fully plastic bending moment method. Zhou et al. [17] and Zhang et al. [18] found the existence of stiffeners could effectively enhance the bond between concrete and steel tubes and reduce the slip, and could give full play to the material properties and increase the overall working performance of the short columns. Ellobody et al. [19] added stiffeners in rectangular and square concrete-filled high-strength stainless-steel tubular columns to study their mechanical properties. The tests showed that the ductility and strength of stiffened stainless-steel tube concrete columns were greatly improved. Lam et al. [20] conducted axial compression tests of square stainless-steel columns filled with concrete (30-100 MPa). The calculation results of the axial compression capacity of concrete-filled steel tube columns were obtained. Gardner et al. [21] conducted a series of axial compression tests of concrete-filled stainless-steel tubes. The tests found that under the same conditions, the axial compression capacity of concrete-filled stainless-steel tubes was higher than that of concrete-filled steel tubes. Uy et al. [22] conducted axial compression and compression-bending mechanical performance tests of concrete-filled stainless-steel tube short columns. The research showed that the mechanical performance was excellent. Subsequently, B. Uy et al. [23] studied the mechanical performance of thin-walled concrete-filled steel tube columns through experiments. The test results showed that the width-to-thickness ratio corresponding to severe buckling of the steel tube was greater than 100. To sum up, scholars had achieved certain results in cold-formed thin-walled steel tubes with different sections and concrete-filled steel tube components [24-29], but there were no research on tubular columns assembled by lipped channels. Two stainless-steel lipped channels were welded to form a new stainless-steel tubular column, with concrete filled inside, a high-performance concrete-filled stainless-steel tubular column was formed.

This paper designed a new type of concrete-filled rectangular thin-walled stainless-steel tubular columns. It had advantages of strong capacity, simple process, and had abundant raw material reserves. Axial compression short column test, finite element analysis of axial compression short columns, axial compression and compression-bending intermediate-length columns were carried in the paper. The key parameters were analyzed, and the recommended calculation method was also proposed.

2. Axial compression test of short columns

2.1. Design and fabrication of specimens

The external casing was composed of two duplex stainless-steel 2205 lipped channels, and the splicing part was equivalent to unidirectional ribs. To prevent the situation of substandard material strength, the strength grade of the infilled concrete was C60 [20]. The fabrication and curing of core concrete was carried out in accordance with the Code GB/T 50081-2002 [30]. The design scheme was shown in Fig.1. The original cross-section was named RA section. The enhanced component cross-section was named RB section. The cold-formed V-shaped ribs were arranged on the long side. The parameters were

shown in Table 1.

Table 1
Parameters of the specimen

Type	H/mm	B/mm	D/mm	R1/mm	R2/mm	t/mm	b_0/mm	b_0/t	A_s/mm^2	A_c/mm^2	b_s/mm
RA	480	160	140	4	4	3	-	-	1942.5	20430.3	-
RB	480	160	140	1	1	3	54	18	2036.9	19537.1	30

Where，A_s-Area of the stainless-steel tube; A_c-Area of concrete inside.

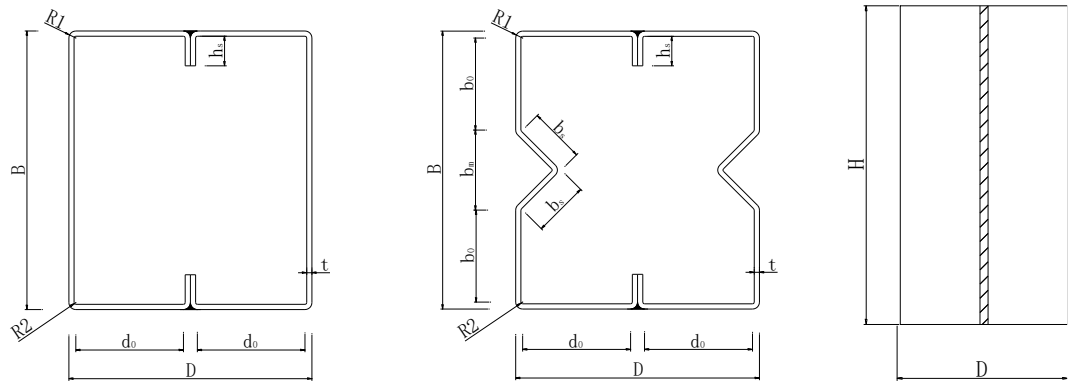

(a) RA section (b) RB section (c) Elevation

Fig. 1 Details of specimens

(a) RA specimens (b) RB specimens

Fig. 2 Processed specimens

Table 2
Actual size of specimens

Specimen	Height H/mm	Section length B/mm	Section breadth D/mm	Average thick-ness of the tube t/mm	Rectangular stiffening ribs length h_s/mm	V-shaped stiffening ribs right-angle edge length b_s/mm	Concrete area A_c/ mm^2	Stainless-steel tube area A_s/ mm^2	Strength and capacity estimate value N_u^i/kN
RA-1	478.5	139.5	161.0	2.83	15.17	-	1832.4	20599.4	2163
RA-2	479.0	140.0	161.5	2.84	16.66	-	1838.9	20743.9	2154
RA-3	479.0	139.5	160.5	2.83	15.67	-	1830.4	20550.4	2160
RB-1	479.0	139.5	160.0	2.79	16.21	30.1	1904.3	19738.7	2515
RB-2	479.0	140.0	159.5	2.84	15.66	30.5	1912.2	19583.8	2517
RB-3	478.5	139.5	160.5	2.83	15.67	30.0	1903.4	19659.6	2520

Before pouring concrete, the actual cross-sectional dimensions of the components were measured first. Fig.2 shows the specimens of the finished preparation. The measured actual cross-sectional dimensions are shown in Table 2.

2.2. Test equipment and loading scheme

2.2.1. Loading equipment

The axial compression test was conducted using a 10,000 kN compression-shear testing machine, as shown in Fig.3. The accuracy of the testing machine was 0.01 kN. The maximum movable distance of the loading end of the testing machine was 450 mm, and the maximum distance between the loading end and the base was 2600 mm. Before the test, it was necessary to set up supports with a height of 1975 mm. Test load and displacement was recorded.

2.2.2. Test equipment and layout of measuring points

The test adopted the DIC-3D 2014a acquisition system, the test equipment and layout of measuring points were shown in Fig.4. The DIC-3D equipment was arranged on the key non-loading surface, and the entire process of component deformation was recorded by the camera. In order to verify the accuracy of the measurement results of the DIC-3D system, four longitudinal strain gauges were arranged and compared with the DIC-3D results. When the strain was large, the strain gauge could only measure the deformation of the initial section. When the deformation is greater than 20,000$\mu\varepsilon$, the strain gauge cannot measure and its results cannot be compared with the results of the DIC-3D [31].

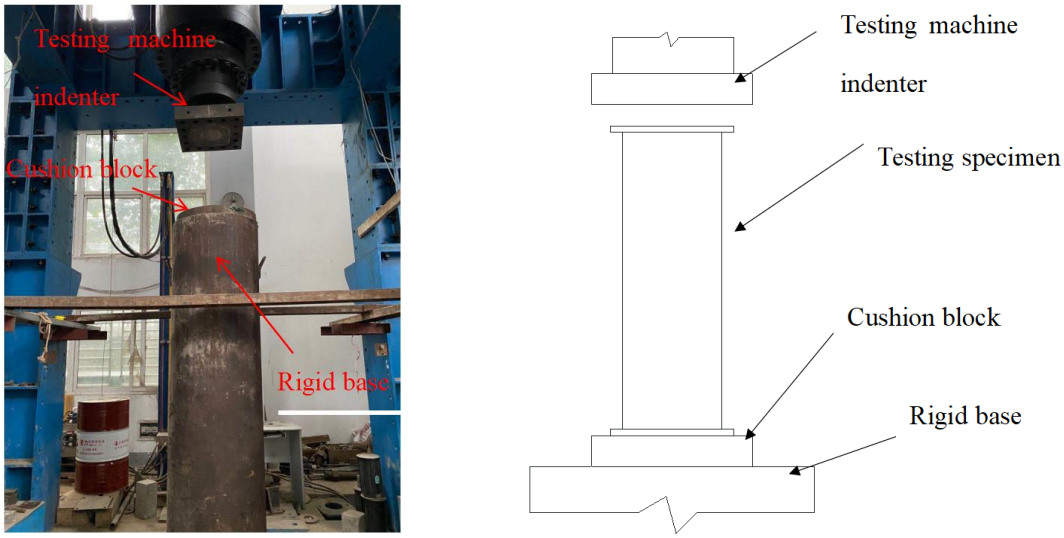

Fig. 3 Loading equipment

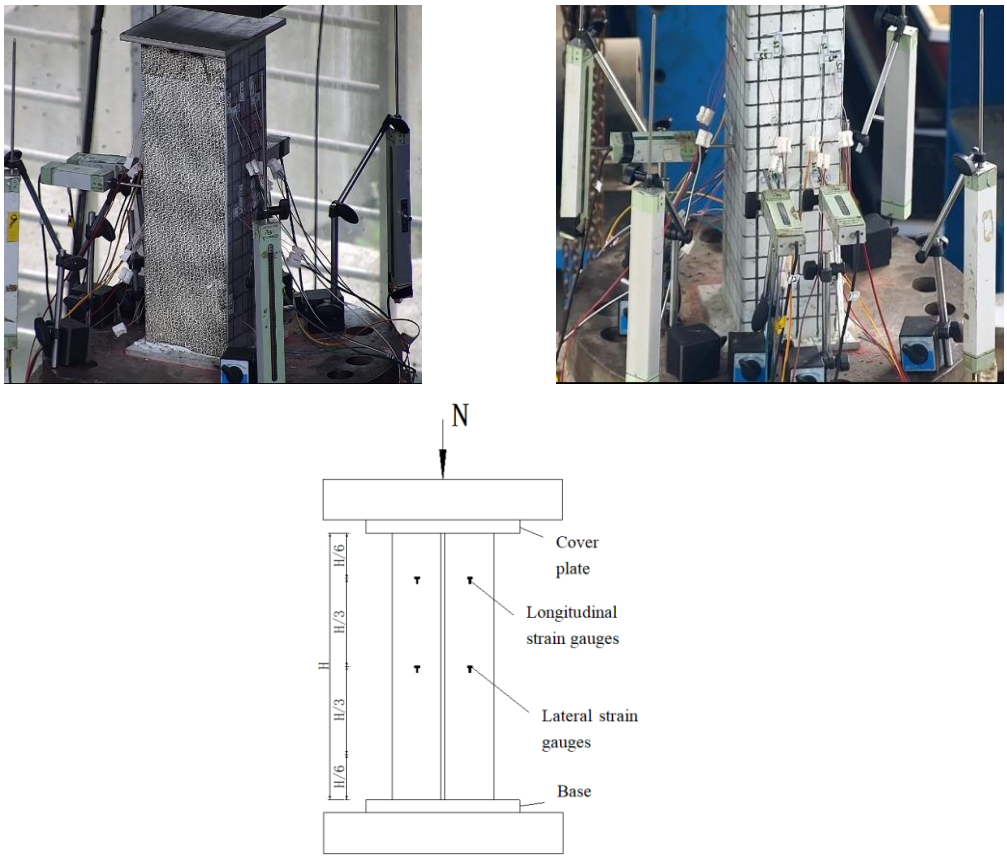

(a) RA specimens

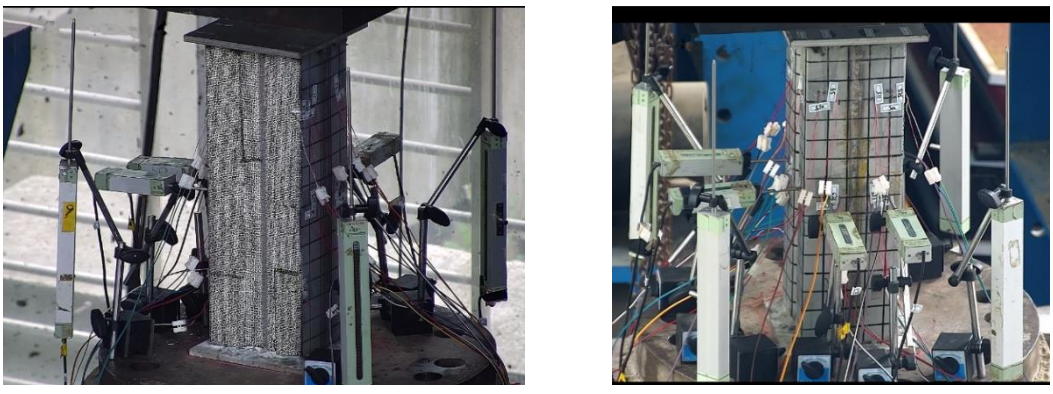

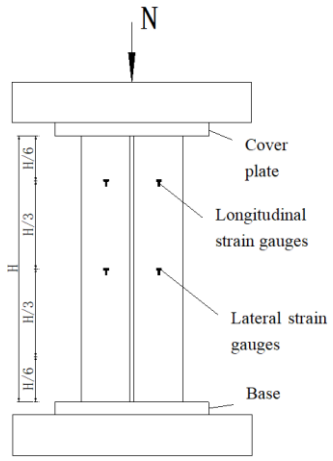

(b) RB specimens

Fig. 4 DIC-3D test equipment and layout of measuring points

Table 3
Detailed loading parameters

Type	Preloading		Stage Ⅰ		Stage Ⅱ			Stage III		Expected total time consumption /min
	Preloading value/kN	Load per level/kN	Ending load /kN	Expected time consumption /min	Load per level/kN	Ending load /kN	Expected time consumption /min	Expected deformation amount/mm	Expected time consumption /min	
RA	110	140	1540	24	110	1980	11	12	6	31
RB	125	160	1760	24	125	2260	9			29

2.2.3. Loading system

The loading scheme adopted the monotonic loading with the combined control of force and displacement, and the loading steps were as follows: (1) Preloading: Preloading to about 5% of the estimated ultimate load to check the stability of the test system and the reliability of the measuring points, and then completely unloaded. (2) First stage: When the load was less than or equal to 70% of the estimated capacity. (3) Second stage: When the load was greater than 70% of the estimated capacity to about 90% of the estimated capacity. (4) Third stage: When the load reached 90% of the estimated ultimate load. The loading parameters of the specific components were shown in Table 3.

2.2.4. Test scheme

The measurement results of the DIC (Digital Image Correlation) equipment were compared with those of the strain gauges and displacement meters to detect the local deformation of the outer wall of the stainless-steel tube during the loading process. The range of the strain gauge was 20,000 (2%). Displacement meters were arranged on the outside and in the middle of the specimen, which were used to measure the longitudinal and transverse total deformations of the specimen respectively. Four displacement meters with a range of 200 mm were arranged on the outside of the specimen, and the displacement meters were parallel to the longitudinal direction of the specimen. The transverse displacement meters were arranged at the H/2 height between the outer cover plate and the bottom plate of the tube wall on the corresponding surface (rectangular rib surface B) of the DIC acquisition system and the adjacent surface of the corresponding surface (non rib surface B or V-shaped rib surface B).

2.3. Test results and analysis

2.3.1. Test process and main phenomena

Fig.5 and Fig.6 showed the situation of concrete spalling after the specimens were cut. The failure mode of the components could be seen in Fig.9-Fig.10. The concrete at the slit did not spall, indicating that the cutting had almost no influence on the actual concrete spalling of the specimens. The failure mode of the internal concrete could clearly represent the state of the specimens after the axial compression test.

For the axial compression short columns of RA and RB in Fig.6, both rectangular stiffeners and V-shaped stiffeners enhanced the restraint capacity of the external stainless-steel tube. The difference was that the failure mode of unidirectional stiffeners was shear failure, while that of bidirectional stiffeners was atypical drum-shaped failure.

Fig. 5 The failure characteristics of RA component

Fig. 6 The failure characteristics of RB component

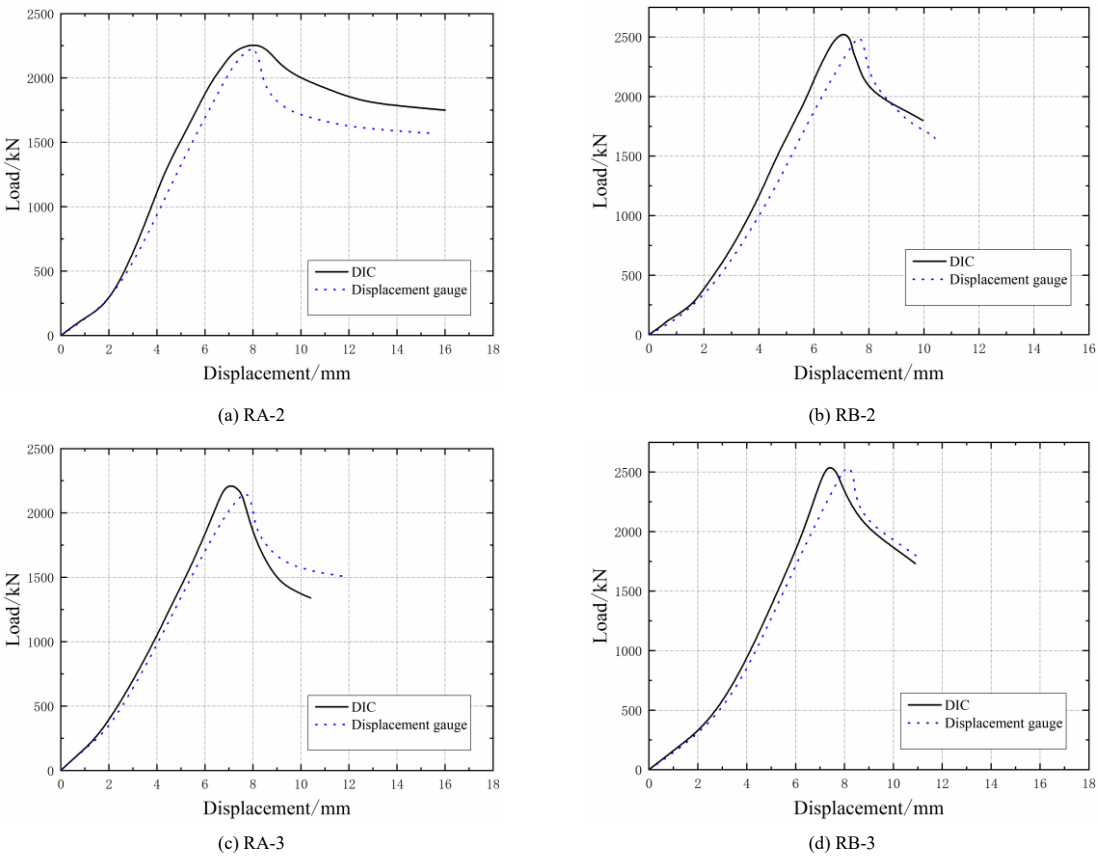

Fig. 7 Comparison of load-displacement curves of experiment and DIC-3D system

Table 4
Comparison of experimental and theoretical values

Specimen	Test value N_{ue}/ kN	Estimate of capacity N'_u/ kN	N'_u/N_{ue}
RA-1	2175	2163	0.994
RA-2	2218	2154	0.971
RA-3	2149	2160	1.005
RB-1	2487	2515	1.006
RB-2	2499	2517	1.007
RB-3	2540	2520	0.992

2.3.2. Test data and analysis

The displacement data obtained from displacement gauges were compared with that of DIC-3D system, as shown in Fig.7. It could be seen that the displacement data of displacement gauges was in good agreement with the DIC-3D system. After calculation, the ultimate capacity of the axial compression short column with bidirectional ribs was 15.04% higher than that of the short column with unidirectional ribs. Stiffeners on the external stainless steel tube changed the buckling state of the component. The unidirectional stiffened component began to buckle when the external stainless-steel tube reached 70% of the ultimate capacity, while the bidirectional stiffened component did not buckle before reaching the ultimate bearing capacity.

2.3.3. Test results

The capacity obtained from the test was compared with the estimated value [26], as shown in Table 4. It was found that the test values agreed well with the theoretical values.

3. Finite element modeling and validation

3.1. Establishment of the FEM

In the verification of the finite element model of the axial compression short column, the stress-strain curves of experiments were adopted and transformed into the true stress-strain curve, as shown in Fig.8. The nominal yield strength f_y was taken as 563 MPa, the elastic modulus E_s was taken as 220087 MPa, and the Poisson's ratio was taken as 0.3 [32]. The concrete and steel pipe grid are 6mm × 6mm, and the end plate grid is 18mm × 18mm. The upper and lower end plates and the high-strength stainless-steel tube were constrained by binding; the upper and lower end plates and the core concrete were in normal "hard" contact; the tube and the core concrete were in "hard" contact. The contact between the tube and the core concrete in the tangential direction, adopted the Coulomb friction model. Considering the surface of the stainless-steel was

relatively smooth and the bonding with the concrete was poor, the interface friction coefficient was taken as 0.2. In ABAQUS analysis, the material with a larger elastic modulus was taken as the master surface in the simulation, and the one with a smaller elastic modulus was taken as the slave surface. Therefore, the high-strength stainless-steel tube was used as the master surface, and the core concrete was used as the slave surface in the simulation. According to the experimental analysis, the straight ribs of the steel tube were in good contact with the core concrete during the failure analysis of the specimen. The straight ribs and the core concrete were constrained by binding (Tie). The weld seams were constrained by binding (Tie). The concrete adopted a plastic damage model with the following parameters: the dilation angle was set to 30° ; the flow eccentricity was 0.1; the ratio of biaxial compressive strength to uniaxial compressive strength was 1.16; the ratio of the second stress invariant in tension to that in compression was 0.667; and the viscosity parameter was set to 0. For the initial geometric defects of median long column compression-bending members, the amplitude calculation was consistent with that of short column under axial compression. The eigenvalue buckling analysis was first carried out, and the lowest-order mode and first-order mode of the analysis results were taken as the initial geometric defects in the model analysis. Considering its overall buckling, the initial geometric defect should also took L/1000 as its overall geometric defect.

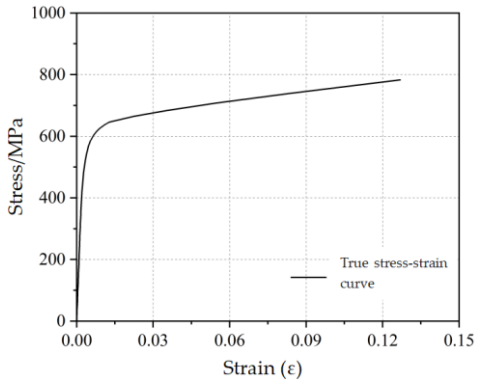

Fig. 8 True stress-strain curve

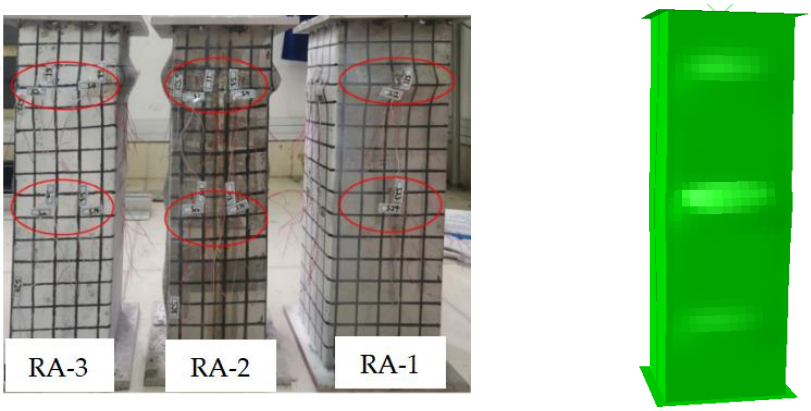

(a) Experiment (b) FEM

Fig. 9 Failure diagram of RA component

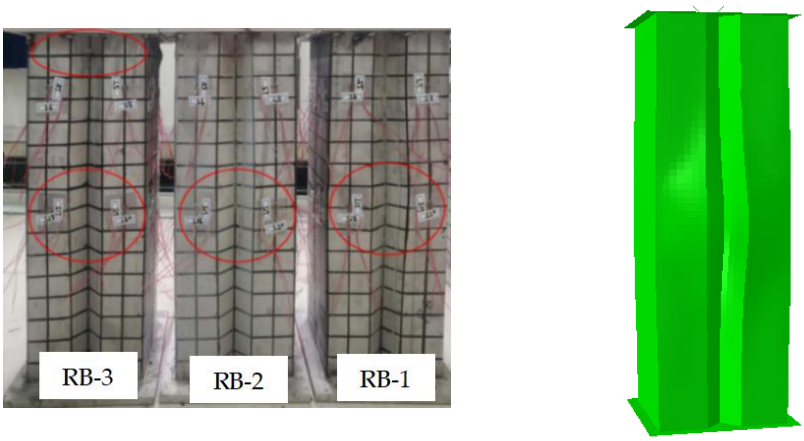

(a) Experiment (b) FEM

Fig. 10 Failure diagram of RB component

3.2. Verification of the FEM

3.2.1. Comparison of failure modes and stress cloud diagrams

At the beginning of the loading, the component was in the elastic stage, and there was no obvious change on the surface of the high-strength stainless-steel tube. As the load increased, when it reached about $0.7N_u$, local buckling occurred in the middle of the RA component. While for the RB component, due to the V-shaped stiffeners, buckling only occurred in the middle of the component when it reached the ultimate capacity. Subsequently, the buckling phenomenon was obvious and the component was damaged, as shown in Fig.9 and Fig.10. The final deformation obtained by FEM (Finite Element Method) was basically consistent with the experiment.

3.2.2. Analysis of the load-displacement curves

Tests and FEM load-displacement curves of RA and RB components were shown in Fig.11. Table 5 listed the ultimate capacities of the two types of components obtained from the experiment and the FEM. Where, N_{exp} represented the ultimate capacity in the experiment, and N_{sim} represented the ultimate capacity in FEM. According to the Table 6, the maximum difference was 8.7%, and the average difference was 4.3%, indicating that the simulation results were reliable. From the failure mode and the load-displacement curve, the finite element model was in good agreement with the experiment, and parameter analysis could be conducted using FEM.

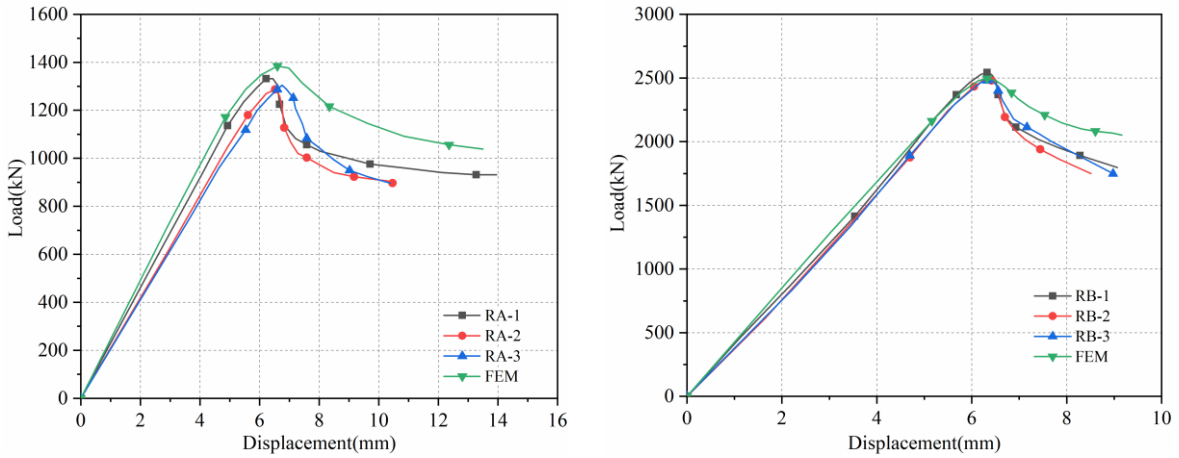

(a) RA type specimens (b) RB type specimens

Fig. 11 Comparison of load-displacement curve

Table 5
Comparison of ultimate capacity between test and FEM

Specimen	Ultimate capacity /kN		N_{exp}/N_{sim}
	N_{exp}/kN	N_{sim}/kN	
RA-1	2175	2355	0.92
RA-2	2218	2355	0.94
RA-3	2149	2355	0.92
RB-1	2487	2492	1.00
RB-2	2499	2492	1.00
RB-3	2540	2492	1.02

4. Numerical analysis of structural performance and compression-bending capacity calculation

4.1. Analysis of axial compression of short columns

4.1.1. Analysis of the loading process

The whole loading process curves of RA and RB components under axial compression load were showed in Fig.12. The peak strain of concrete was about 0.004, which was much larger than the peak strain of 0.0024 of plain concrete under uniaxial compression. The axial compression peak strains corresponding to RA and RB components were 0.00347 and 0.00409 respectively, and the axial compression ultimate capacities were 2355.8 kN and 2497.7 kN. The ultimate capacity was increased by 6.0%. It showed that compared with RA components without stiffeners, the V-shaped stiffeners of RB components had a stronger ability to confine the core concrete and could better improve the ultimate capacity of axial compression. In the descending section, the curve of RB components was gentler compared with that of RA, indicating that V-shaped stiffeners could improve the ductility.

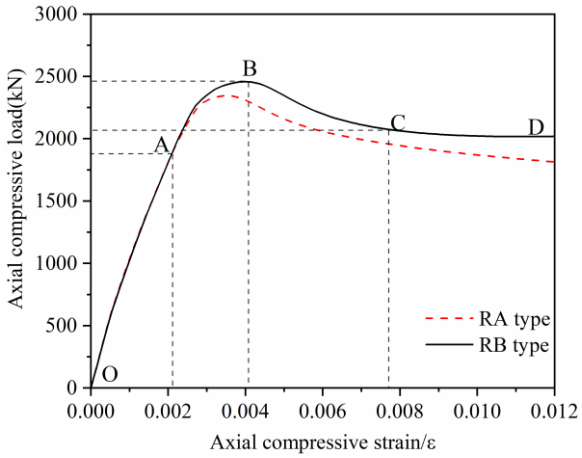

Fig. 12 Axial load-strain relationship curves of RA and RB members

4.1.2. Analysis of the concrete cross-section performance

The greater the lateral restriction provided by the high-strength stainless-steel tube was, the larger the range of the effective confined zone of the core concrete was. Fig.13 showed the Mises stress distribution nephogram of the middle section of the concrete of RA and RB components at the ultimate load. The lateral restriction of RA was mainly concentrated at the corners, right-angle ribs and the center of the section. The diagonal confined zone was synthesized along two directions relying on the stiffness of the right-angle ribs and corners. The lateral restriction of RB was mainly distributed at the corners, right-angle ribs, the corners of V-shaped stiffeners and the center of the section, and the area of the middle confined zone was larger than that of the cross-section of RA, which was about twice the area of the middle confined zone of RA component.

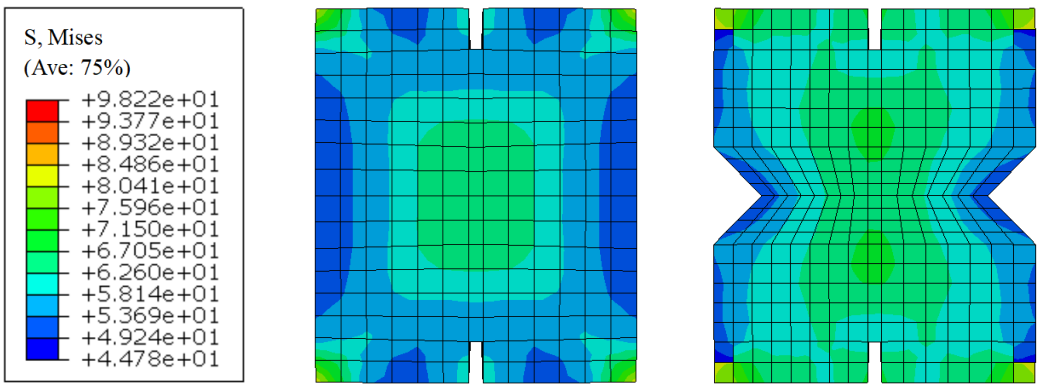

(a) RA specimens (b) RB specimens

Fig. 13 Stress nephogram of middle section of the core concrete

4.1.3. Analysis of the interface performance between stainless-steel and concrete

When the axial load was small, the high-strength stainless-steel tube and the concrete remained in a bonding state and had good contact. As the axial load increased, gaps began to appear. The gaps mainly occurred at the surface and V-shaped stiffener, while the corners and right-angle ribs still maintained a good contact relationship. The cross-sections of RA and RB short columns reaching the ultimate capacity were shown in Fig.14, where P is the midpoint on the edge of the non-ribbed surface (RA) and the V-shaped stiffener surface (RB) of the mid-span section of the short column. The non-ribbed surface of the middle section of the RA short column had already undergone visible bulging, while the RB was not obvious, and at the later stage of loading, the tube and the concrete were separated at P. The deformation and failure of the short column were caused by the buckling of the stainless-steel tube in the middle and the transverse deformation. The relationship between the contact gap and the longitudinal displacement at point P of the RA and RB short columns was shown in Fig.15. At the initial stage of loading, the contact gap of the two types of components remained zero at P. When the ultimate capacity was reached, the contact gap between the tube and the concrete of RA reached 1.68 mm, while the contact gap of RB was only 0.48 mm, indicating that the V-shaped stiffener could greatly alleviate the buckling of the high-strength stainless-steel tube.

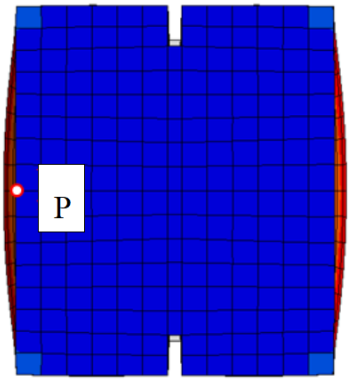

(a) RA type specimens

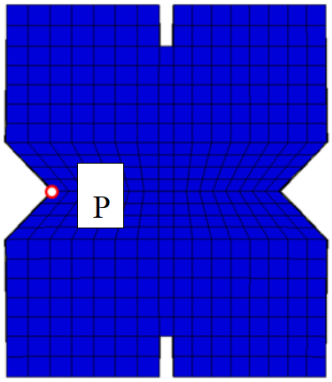

(b) RB type specimens

Fig. 14 Deformation of mid-span section of short column

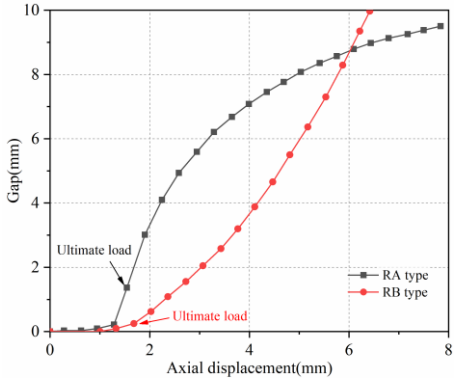

Fig. 15 Contact gap-displacement curve of P point

4.1.4. Analysis of the influence of main parameters

This section conducted a parameter analysis taking the size of the V-shaped stiffeners (including the angle φ and depth h_v), the strength of the core concrete, and the width-thickness ratio of the plate b_0 / t as variables, as shown in Fig.16.

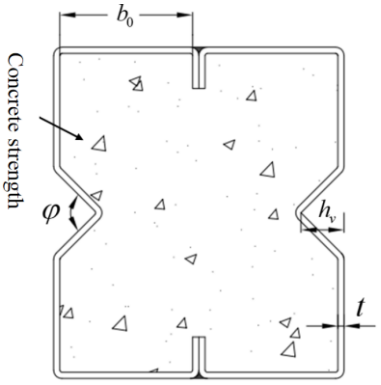

Fig. 16 Details of V-stiffener size

Where, φ were taken as 30°, 45°, 60°, 90°, and 120°, and h_v were taken as 18mm, 19mm, 20mm, 22mm, 24mm, 27mm and 30mm. Fig.17 showed the depth-ultimate load relationship curves of different depths h_v of V-shaped stiffeners. When the angles of V-shaped stiffeners φ were 30°, 45°, and 60° respectively, the ultimate load increased with the increase of the depth. When φ was 90°, the ultimate load slightly decreased with the increase of the depth. While when φ was 120°, the ultimate load decreased rapidly with the increase of the depth. The reason was that: with the continuous increase of the load, the entire component entered the elastic-plastic stage. The Poisson's ratio of the concrete was greater than that of the stainless-steel tube, the transverse deformation of the concrete was greater than that of the stainless-steel tube, and the concrete exerted lateral pressure on the steel tube. When φ was 120°, even if the minimum stiffness of the V-shaped stiffener met the requirements, it was not conducive to improving the stiffness of the steel tube. Compared with the V-shaped stiffeners with small angles, it was more likely to bulge outward under the action of lateral load, indicating that the use of 120° V-shaped stiffener could not effectively improve the confinement effect on the concrete. When the depth was less than 20mm, the section performance increased with the increase of the depth of the V-shaped stiffener. When the depth was greater than 20mm, the section performance decreased with the increase of the depth of the V-shaped stiffener. In particular, when the angle was 90°, the section performance dropped rapidly. After the depth exceeded 25mm, the section performance was lower than that of the 60° section. When the angle of the V-shaped stiffener was 120°, the section performance at any depth was far lower than that of other angles. Therefore, in actual engineering design, angles greater than 90° were avoided.

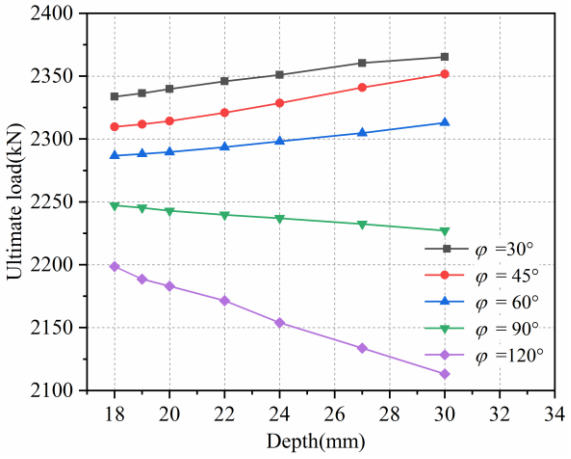

Fig.17 Relationship between V-shaped stiffener depth and ultimate load

Fig.18 showed the relationship between different angles of V-shaped stiffeners and ultimate loads. As φ increased, the ultimate load of the component continuously decreased. The greater h_v, the greater the degree of decrease in the ultimate load. When the depth h_v was small (18-20mm), the

smaller the angle, the smaller the stiffness of the V-shaped stiffener, resulting in a relatively low ultimate capacity. When h_v was small (22-30mm), the larger the angle, the greater the weakening degree of the V-shaped stiffener on the component section, also resulting in a relatively low ultimate capacity. After analysis, the optimal size of the V-shaped stiffener was a depth of 20mm, that is, the width-thickness ratio of the V-shaped stiffener plate was 8.33, and the angle was 90°.

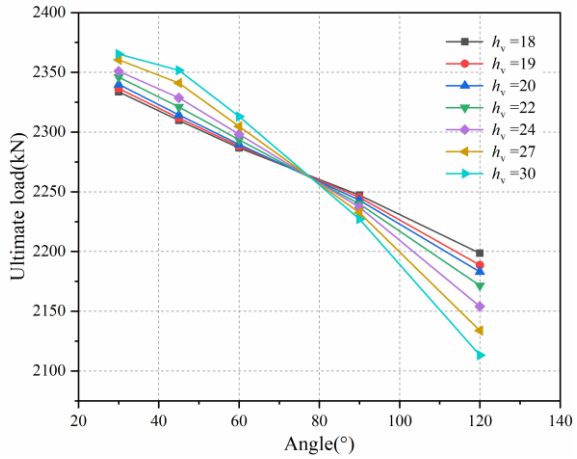

Fig. 18 Relationship between V-shaped stiffener angle and ultimate load

On the basis of determining the size of the V-shaped stiffener, different strengths of high-strength concrete were selected as parameters to analyze their applicability with high-strength stainless-steel tubes, in order to give full play to the mechanical properties of both. The high-strength concrete was taken as C60 to C80 respectively, with a total of 5 sets of components. The specific parameter information was shown in Table 6. The components were assigned according to R-concrete strength. For example: R-C60 indicated that the component had a concrete strength of C60. After analysis, the peak load corresponding to C60 was 2242 kN, and the peak load corresponding to C80 was 2628 kN, with an increase of 17.20%. Fig.19 showed the axial forces by the stainless-steel tube and the concrete under different strengths.

Table 6
Details of concrete strength

Speci-men	*H*/ mm	*B*/m m	*D*/ mm	*t*/ mm	Con-crete grade	f_{ck}/MPa	f_c'/MPa	N_u/kN
RB-60					C60	38.5	49.97	2242.93
RB-65					C65	41.5	54.90	2336.75
RB-70	480	160	140	3	C70	44.5	60.98	2435.78
RB-75					C75	47.5	64.98	2532.10
RB-80					C80	50.2	69.97	2628.77

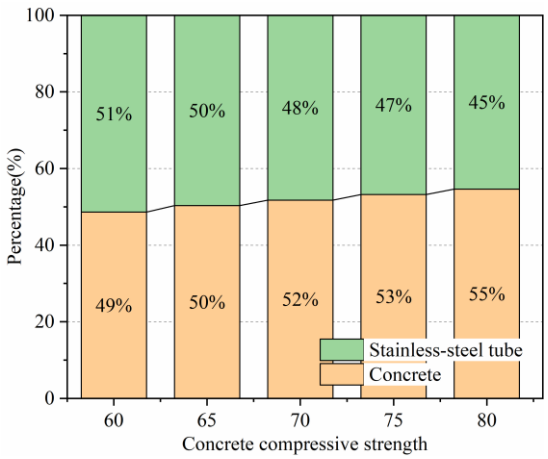

Fig. 19 Ratio of stainless-steel tube to concrete capacity

Different stainless-steel tube thicknesses were chosen to study the influence of different width-thickness ratios of the plate on the axial compression performance of the short columns. The thicknesses were taken as 2.0mm, 2.5mm, 3.0mm, 3.5mm, and 4.0mm. Fig.20 showed the ratio of the average stress of the tube section to the yield strength for different width-thickness ratios of the plate. When the width-thickness ratio was between 18 and 21.3, the average stress of the tube section could reach 0.95 f_y, indicating that the tube could better exert its material properties at this time. Therefore, the width-thickness ratio was recommended to be 18-21.3.

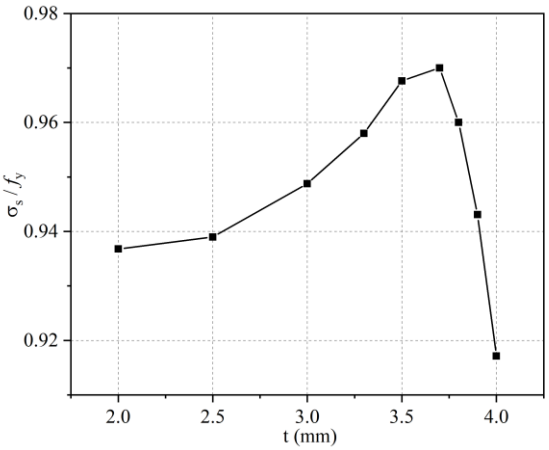

Fig. 20 Ratio of average stress to yield strength of steel tube section with different width-to-thickness ratio of plates

4.2. Analysis of axial compression and compression-bending of intermediate-length columns

4.2.1. Analysis of the concrete cross-section performance

The influence of eccentric load on the cracking of core concrete in medium-long columns was analyzed by the maximum principal plastic strain PEEQ in ABAQUS, as shown in Fig.21. When the eccentric load was $0.25N_u$, the maximum principal plastic strain PEEQ was basically 0, indicating that the core concrete did not crack at this time. When the eccentric load reached $0.63N_u$, tiny cracks occurred near the middle section of the eccentric load, and the component began to enter the elastic-plastic stage. With the continuous increase of the eccentric load, the plastic principal strain of the concrete at the middle section continuously expanded towards the neutral axis, and the component bent significantly in the eccentric direction. When the ultimate eccentric load was reached, the middle section of the concrete part basically cracked.

4.2.2. Analysis of the interface performance between stainless-steel and concrete

Fig.22 was the middle section view of the component, and a limited number of 1 to 9 nodes were selected to analyze the interface characteristics between the high-strength stainless-steel tube and the concrete. The initial gap at the interface between the stainless-steel and the concrete was 0, and the contact pressure was 0. With the increase of the eccentric load, the initial Poisson's ratio (0.3) of the tube was greater than the initial Poisson's ratio (0.2) of the concrete, a gap was generated between the tube and the concrete, and the restraint effect of the concrete by the tube also began to decrease. Fig.23 showed the change process of the gap between the stainless-steel and the concrete at each node of the middle section of the high-strength stainless-steel tube concrete component with the increase of the load. When the longitudinal displacement reached about 0.7mm, the tube and the concrete at the middle section of the V-shaped stiffener surface began to separate. With the increase of the longitudinal displacement, the separation distance between the tube and the concrete at points 4 and 6 of the V-shaped stiffener surface was the most obvious, and there was also a certain separation at point 5. When the longitudinal displacement reached about 3mm, that is, when the ultimate load was reached, the tube and the concrete at the middle section of the right-angle rib surface were basically not separated, while the separation gap at the V-shaped stiffener surface was large, about 2.5mm. When the longitudinal displacement reached about 0.7 mm, the stainless steel tube and concrete at the corners (Points 3 and 7) of the middle section of the stainless steel tube concrete component began to squeeze each other, generating contact pressure. As the longitudinal displacement increased, the contact pressure at the corners increased rapidly. When the longitudinal displacement reached 3 mm, that is, when the bending pressure load reached the ultimate load, the contact pressure at Corners 3 and 7 was the greatest. The contact pressure at the corner (Point 3) of the middle section in the compression zone reached 37 MPa, the contact pressure at the corner (Point 7) of the middle section in the

tension zone reached 25 MPa, and the contact pressure at Point 1 of the middle section in the compression zone of the right-angle rib surface reached 2.9 MPa. Compared with the corner contact pressure, the facial contact pressure was very small and could be ignored.

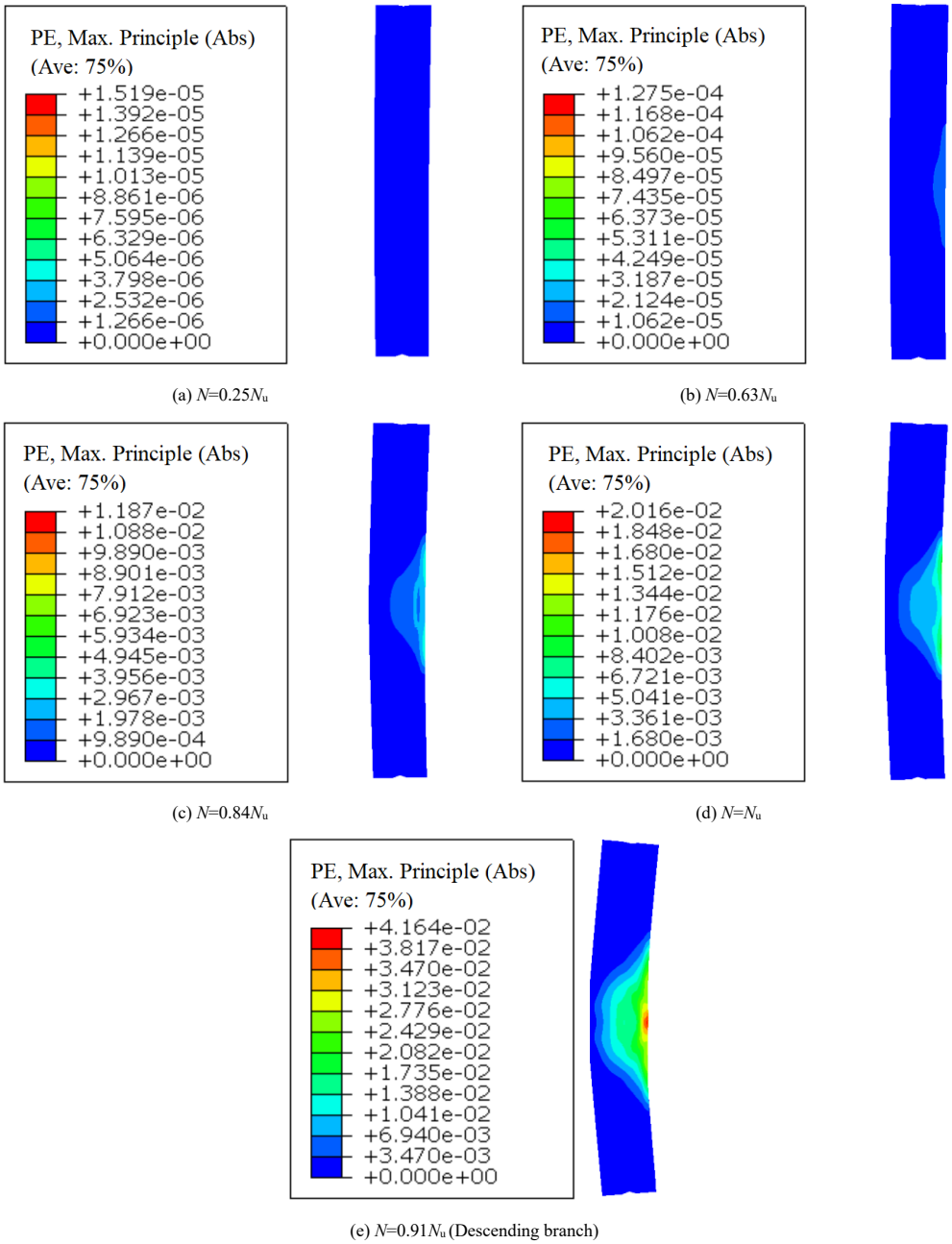

(a) N=0.25N_u (b) N=0.63N_u

(c) N=0.84N_u (d) N=N_u

(e) N=0.91N_u (Descending branch)

Fig. 21 Finite element prediction of cracks and crushing of concrete filled in members

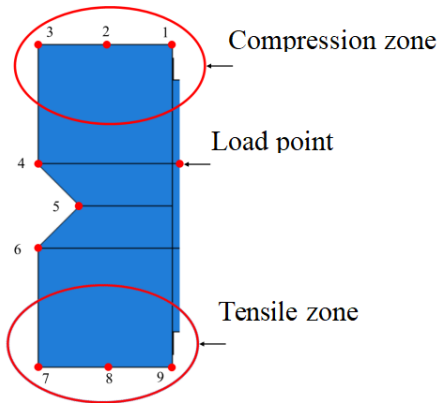

Fig. 22 The middle section of the component

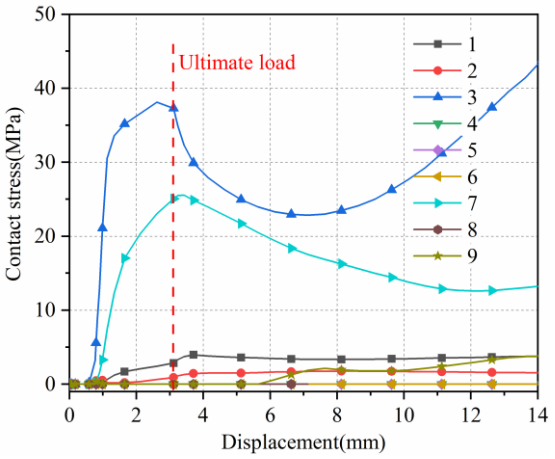

Fig. 23 Relationship of displacement-contact stress of each node in the middle section

4.2.3. Analysis of the influence of main parameters

The corresponding eccentricities were 0, 0.19, 0.38, 0.56, 0.75, 0.94, 1.25, 1.875, 2.5 and 3.75. When the eccentricity was small (e = 0.19), the middle section of the component was entirely in a compressive state. As the eccentricity increased (e = 1.0), the compressive zone of the middle section of the component decreased, and there was a tendency for tension in the direction away from the eccentricity. When the eccentricity increased to 1.25, a tensile zone appeared in the direction of the component away from the eccentricity. When the eccentricity (e = 3.75) was large, the tensile zone of the middle section of the component expanded. At this time, the range of the tensile zone was basically consistent with that of the tensile zone, and the component undergone compressive failure in the compressive zone and tensile failure in the tensile zone. Fig.24 showed the influence of the eccentricity on the ultimate compression-bending capacity of intermediate-length columns. When the eccentricity was less than 0.5, the ultimate compression-bending capacity decreased rapidly. When the eccentricity was greater than 1, the ultimate compression-bending capacity decreased slowly. When the section properties of the components were the same, the larger the slenderness ratio was, the gradually smaller the influence of the eccentricity on the ultimate compression-bending capacity was.

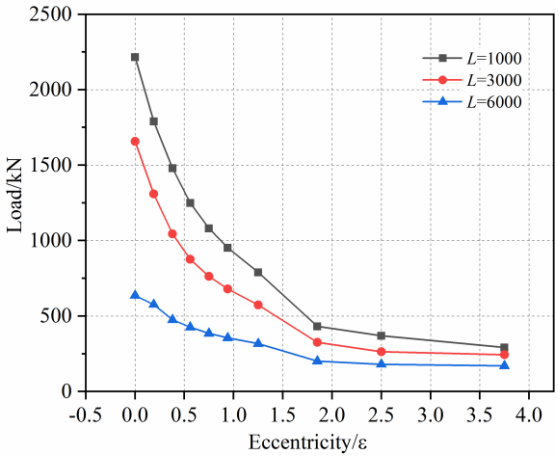

Fig. 24 Effect of eccentricity on ultimate capacity of members

The slenderness ratio was chosen as 15.17, 30.34, 45.51, 60.68, 75.85 and 91.02. The influence of the slenderness ratios was shown in Fig.25. For the same concrete-filled high-strength stainless-steel tubular columns, the peak compression-bending load decreased with the increase of the slenderness ratio. The smaller the slenderness ratio, the faster the peak compression-bending load decreased. Under the same eccentricity, the peak compression-bending load of concrete-filled high-strength stainless-steel tube columns decreased approximately linearly with the increase of the slenderness ratio, and the smaller the eccentricity, the steeper the decrease of the peak compression-bending load. When the eccentricity was 300mm, the peak compression-bending load remained basically unchanged.

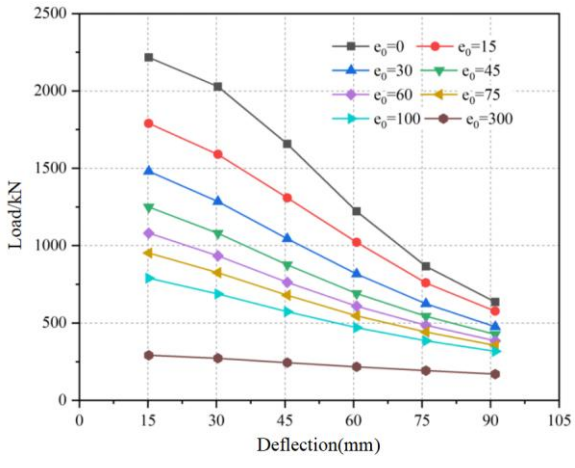

Fig. 25 The change of bending peak load with slenderness ratio

The thicknesses of the stainless-steel tubes were taken as 2mm, 3mm, and 4mm, and the width-thickness ratios of the sub-plates were 33.0, 21.3, and 15.5 respectively. Analyze the influence of the width-thickness ratio, as shown in Fig.26. For the same concrete-filled high-strength stainless-steel tubular column, the peak compression-bending load decreased with the increase of the width-thickness ratio. The smaller the width-thickness ratio of the plate, the faster the peak compression-bending load decreased. Under the same eccentricity, the peak compression-bending load decreased approximately linearly with the increase of the width-thickness ratio of the plate, and the smaller the eccentricity, the steeper the decrease of the peak compression-bending load. When the eccentricity was 300mm, the peak compression-bending load remained basically unchanged.

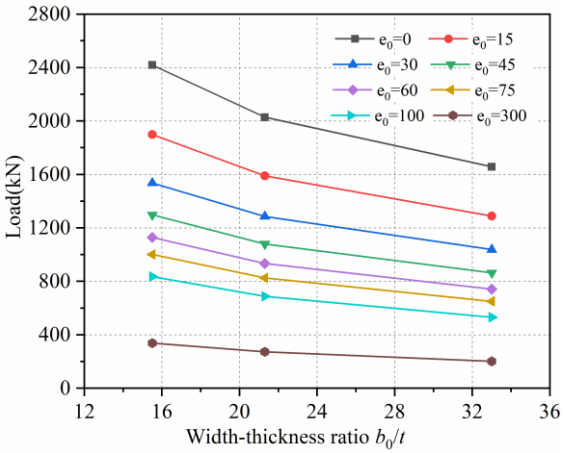

Fig. 26 The change of bending peak load with width-thickness ratio of plate

4.3. Recommendation of compression-bending capacity calculation formula

For the concrete-filled high-strength stainless-steel tubular column, the compression-bending capacity by the Chinese code T/CECS 952 and FEM was calculated. Results showed the dispersion rate between Chinese code T/CECS 952 and finite element calculation results was only 0.06. Therefore, the design formula of the Chinese code T/CECS 952 was modified to make it applicable to the calculation of the compression-bending capacity of median long column with sorbite high-strength stainless-steel S600E (f_y = 600MPa). Fig.27 showed a typical N/N_u-M/M_u relationship curve of concrete-filled stainless-steel tube. There was an equilibrium point C (ζ_0, η_0). With the increase of the slenderness ratio, the equilibrium point C (ζ_0, η_0) became more and more concave and less and less obvious. The main reason was that the influence of the second-order effect became more and more obvious with the increase of the slenderness ratio.

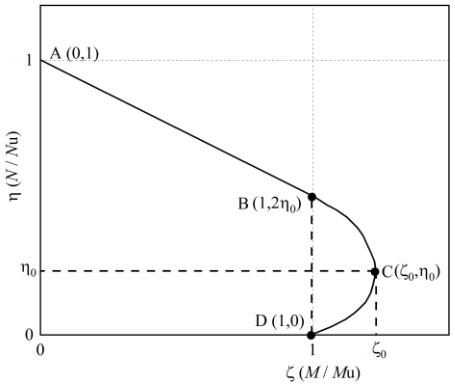

Fig. 27 Typical N/N_u-M/M_u relationship curve

Referred to the Chinese code T/CECS 952, ζ_0, η_0 in the equilibrium point C(ζ_0, η_0) could be approximately expressed as a function of the restraint effect ξ . A linear regression analysis was conducted and the corresponding functional relationship was obtained. For high-strength concrete-filled stainless-steel S600E tubular column, it could be calculated according to Eqs.(1) and (2).

$$\varsigma_0=1+0.11\xi^{-1.15} \quad (1)$$

$$\eta_0=0.1+0.09\xi^{-0.76} \tag{2}$$

The equation suggested in this paper still adopted a two-segment function for representation. Considering the influence of the slenderness ratio, the N/N_u-M/M_u equation of the median long column of concrete-filled high-strength stainless-steel tube could be expressed as Eq.(3).

$$\begin{cases} \dfrac{N}{\varphi\cdot N_u}+(\dfrac{a}{d})\cdot\dfrac{M}{M_u}=1 & \dfrac{N}{N_u}\geq 2\varphi^3\cdot\eta_0 \\ \dfrac{-b\cdot N^2}{N_u^2}-\dfrac{c\cdot N}{N_u}+(\dfrac{1}{d})\dfrac{M}{M_u}=1 & \dfrac{N}{N_u}\leq 2\varphi^3\cdot\eta_0 \end{cases} \tag{3}$$

The comparison between the ultimate capacity of the compression-bending median long column calculated by the proposed calculation method and the finite element calculation results was shown in Fig.28. It could be seen the proposed calculation method was reliable.

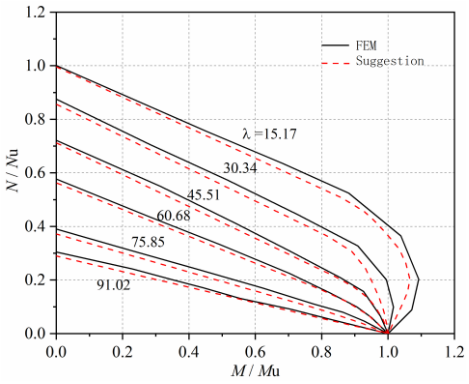

(a) Influence of slenderness ratio on N/N_u-M/M_u curve

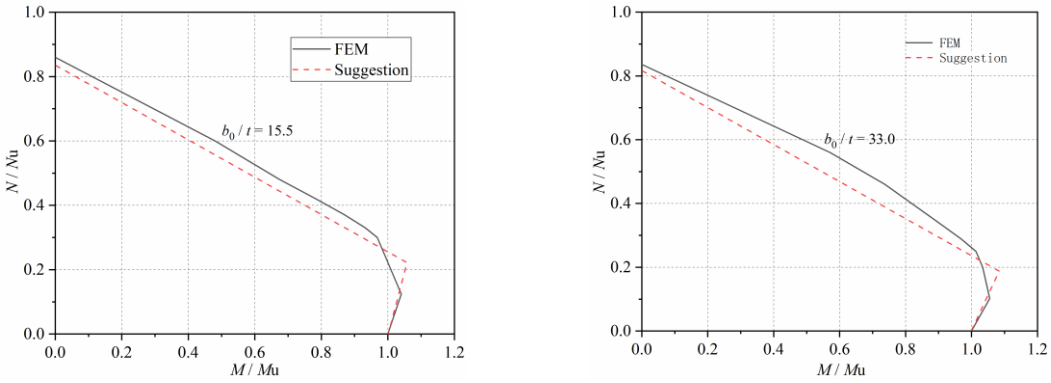

(b) Influence of the width-thickness ratio on the N/N_u-M/M_u curve

Fig. 28 Comparison of N/N_u-M/M_u relationship between the proposed method and FEM

Fig.29 showed the comparison between the proposed calculation method for S600E concrete-filled high-strength stainless-steel tubular columns and the finite element calculation results. Among them, N_{ue} represented the result of the ultimate compression-bending capacity calculated by the finite element method, and N_{u1} represented the result of the ultimate compression-bending capacity calculated by the proposed calculation method. $\overline{x}$ was the average value of N_{ue}/N_{u1}, and σ was the standard deviation of N_{ue}/N_{u1}. Through the comparison, the finite element results of the other components were all slightly smaller than the results of the proposed calculation method. Through calculation, the average value of N_{ue}/N_{u1} for concrete-filled high-strength stainless-steel tubular columns was 1.06, and the standard deviation of N_{ue}/N_{u1} was 0.035. It indicated that the proposed calculation method for calculating the compression-bending capacity was conservative.

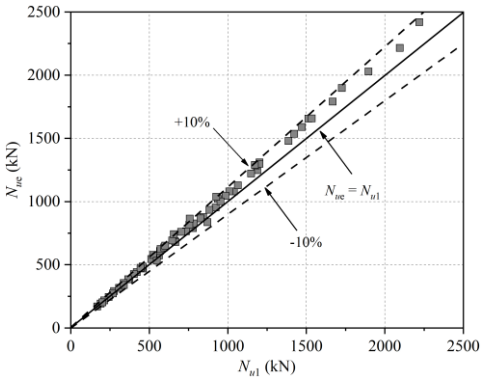

Fig. 29 Comparison between the proposed calculation method and FEM

5. Conclusions

This paper aimed at the environmental requirements of marine engineering. With the purpose of delaying the local buckling of the pipe wall and improving the restraint effect of the core concrete, two new types of concrete-filled thin-walled high-strength stainless-steel tubular columns were designed, the structural performances were studied by experiments and FEM. The main conclusions were as follows:

(1) Stiffeners on the external stainless-steel tube effectively improved the capacity of the axial compression short column. The ultimate capacity of the axial compression short column with bidirectional stiffeners was 15.04% higher than that of the axial compression short column with unidirectional stiffeners.

(2) The most important parameters affecting the axial compression short columns were the size of the V-shaped stiffeners and the strength of the concrete. When the width-thickness ratio of the V-shaped stiffeners was 8.33 and the angle was 90°, the size of cross-section was optimal. When the concrete was C80, the peak load was increased by 17.20% compared with C60.

(3) The most important parameters affecting the axial compression and compression-bending intermediate-length columns were the slenderness ratio and the eccentricity. When the slenderness ratio was between 15.17 and 91.02, the larger the slenderness ratio, the faster the stiffness degradation. When the eccentricity was between 0.56 and 3.75, the column had better deformation capacity and better ductility.

(4) The recommended calculation formula for the compression-bending capacity of medium long columns of concrete-filled thin-walled high-strength stainless-steel tubular columns was proposed, with high accuracy.

Reference

[1] Ayough P, Sulong NHR, Ibrahim Z. Analysis and review of concrete-filled double skin steel tubes under compression. Thin-Walled Struct 2020;148:106495.
[2] Shao ZW, Zha XX, Wan CY. Design method of fire-resistance capacity of reinforced-concrete-filled steel tube column under axial compression. Fire Saf J 2022;129:103572.
[3] Ukanwa KU, Clifton GC, Lim JB, et al. Simple design procedure for concrete filled steel tubular columns in fire. Eng Struct 2018;155:144-156.
[4] Duarte APC, Silva BA, Silvestre N, et al. Tests and design of short steel tubes filled with rubberised concrete. Eng Struct 2016;112:274-286.
[5] Tan QH, Gardner L, Han LH, et al. Fire performance of steel reinforced concrete-filled stainless steel tubular (CFSST) columns with square cross-sections. Thin-Walled Struct 2019;143:106197.
[6] Wang J, Yang Z, Zheng X. Axial compression behavior of square section concrete- filled steel tubes reinforced with internal latticed steel angles. J Constr Steel Res 2024;213:108414.
[7] Chen Z, Zhou J, Jing C, et al. Mechanical behavior of spiral stirrup reinforced concrete filled square steel tubular columns under compression. Eng Struct 2021;226:111377.
[8] Wu LL, Han GH, Sarno LD, et al. Experimental and numerical analysis of L-shaped concrete-filled steel tube stub columns. Structures 2024;69:107351.
[9] Ren QX, Zhou KZ, Li W. Experimental study of clay concrete filled steel tubular stub columns under axial compression. Structures 2024;70:107509.
[10] Chen J, Song SS, Ye J, et al. Axial compressive behaviour and design of concrete-filled wire arc additively manufactured steel tubes. Structures 2024;70:107495.
[11] Ahmed M, Shahin RI, Yehia SA, et al. Nonlinear analysis of square steel-reinforced concrete-filled steel tubular short columns considering local buckling. Struct Concr 2024;1:69-84.
[12] Hu JY, Huang YF, Li WJ, et al. Compressive behaviour of UHPC-filled square high-strength steel tube stub columns under eccentric loading. J Constr Steel Res 2022;198:107558.
[13] Ukanwa KU, Clifton GC, Lim JB, et al. Simple design procedure for concrete filled steel tubular columns in fire. Eng Struct 2018;155:144-156.
[14] Lai ZM, Varma AH, Noncompact and slender circular CFT members: Experimental database, analysis, and design. J Constr Steel Res 2014;101:455-468.
[15] Aslani F, Uy B, Tao Z, Predicting the axial load capacity of high-strength concrete filled steel tubular columns. Steel Compos Struct 2015;19:967-993.
[16] Liew JYR, Xiong M, Xiong D, Design of concrete filled tubular beam-columns with high strength steel and concrete. Structures 2016;8:213-226.
[17] Zhou XH, Liu YJ, Jiang L, Review of the mechanical properties of PBL reinforced rectangular concrete filled steel tube structure. Journal of Chinese Highway 2017;30:45-62.
[18] Zhang N, Liu YJ, Li H, Analysis of local flexion performance of PBL stiffening rectangular concrete filled steel tube. Journal of Building Science and Engineering 2017;34:95-102.
[19] Ellobody E, Nonlinear behavior of concrete-filled stainless steel stiffened slender tube columns. Thin-Walled Struct 2007;45:259-273.
[20] Lam D, Gardner L, Structural design of stainless steel concrete filled columns. J Constr Steel Res 2008;64:1275-1282.
[21] Zhang WF, Gardner L, Wadee MA, On the uniform torsional rigidity of square concrete-filled steel tubular (CFST) sections. Structures 2022;43:249-2521.
[22] Tao Z, Uy B, Analysis and design of concrete-filled stiffened thin-walled steel tubular columns under axial compression. Thin-Walled Struct 2009;47:1544-1556.
[23] Uy B, Strength of concrete filled steel box columns incorporating local buckling progress of building steel structure. J Struct Eng 2003;126:341-352.
[24] Liao JJ, Zeng JJ, Long YL, et al. Behavior of square and rectangular concrete-filled steel tube (CFST) columns with horizontal reinforcing bars under eccentric compression. Eng Struct 2022;271:114899.
[25] Lin L, Wang FC. Investigation of analytical behavior of concrete filled steel tubular (CFST) offshore rock-socketed pile under lateral load. Ocean Eng 2023;277:114279.
[26] Cai YC, Su MN, Chen XR, et al. High strength steel square and rectangular tubular stub columns infilled with concrete. J Constr Steel Res 2021;179:106536.
[27] Lin SQ, Li ZL, Zhao Y. Behavior of eccentrically loaded circular concrete-filled steel tube stub columns with localized corrosion. Eng Struct 2023;288:116227.
[28] Tang HY, Wang HX, Liu Y, et al. Axial compressive property of square and rectangular UHPC-filled duplex stainless steel tube stub columns. Compos Struct 2023;323:117492.
[29] Tang HY, Hou LJ, Yuan ZJ, et al. Eccentric compressive behavior of square concrete-filled stainless steel tube (CFSST) stub columns. Struct 2023;55:1920-35.
[30] GB/T 50081-2002. Standard for test method of mechanical properties on ordinary concrete. Beijing, China: Standard Press of China; 2002.
[31] Peng Y, Zhao J, Chen LS, et al. Residual stress measurement combining blind-hole drilling and digital image correlation approach. J Constr Steel Res 2021;176:106346.
[32] Huang YQ, Yang JJ, Feng RQ, et al. Resistance of cold-formed sorbite stainless steel circular tubes under uniaxial compression. Thin-Walled Struct 2022;179.